


Article

Performance Analysis of the Structures Using Glass-Fiber-Reinforced-Polymer-Produced Hollow Internal Molds

Zhenhao Zhang , Zanke Yang *, Hesheng Li and Weijun Yang

School of Civil Engineering, Changsha University of Science and Technology, Changsha 410114, China; zhangzhenhao@csust.edu.cn (Z.Z.); 21202030479@stu.csust.edu.cn (H.L.)

* Correspondence: 21202030549@stu.csust.edu.cn

Abstract: Hollow structures reduce weight without compromising load-bearing capacity and are widely used. The new Glass-Fiber-Reinforced Polymer high-strength thin-walled inner mold simplifies internal cavity construction and boosts structural performance. This study first investigates the influence of a GFRP high-strength thin-walled circular tube on the cross-sectional load-carrying capacity of hollow slabs. Then, a formula for the bending load-carrying capacity of the section under the action of the tube is derived. The results indicate that when the height of the concrete compression zone meets certain conditions, GFRP high-strength thin-walled circular tubes can improve the ultimate load-carrying capacity of the hollow floor slabs. In order to achieve a more economical design, the bending moment modification of a GFRP high-strength thin-walled circular tube of a continuous slab was studied. Research has found that the bending moment modulation limit for a continuous slab is 35.65% when it is subjected to a load of $P_u = 24$ kN. Experimental analysis has shown that the results are generally consistent with the calculations. In practical engineering, the application of a GFRP high-strength thin-walled circular tube of continuous slabs has limitations. Therefore, this study investigated a GFRP high-strength thin-walled honeycomb core slab and found that its ultimate load-bearing capacity is greater compared to waffle slabs. In addition, the stress performance of the GFRP high-strength thin-walled honeycomb core internal mold is superior, making it more promising for practical applications.

Keywords: hollow structures; GFRP; high-strength thin-walled circular tube; high-strength thin-walled honeycomb core slab; structural performance



Citation: Zhang, Z.; Yang, Z.; Li, H.; Yang, W. Performance Analysis of the Structures Using Glass-Fiber-Reinforced-Polymer-Produced Hollow Internal Molds. *Buildings* **2024**, *14*, 1319. <https://doi.org/10.3390/buildings14051319>

Academic Editor: Duc-Kien Thai

Received: 26 March 2024

Revised: 13 April 2024

Accepted: 2 May 2024

Published: 7 May 2024



Copyright: © 2024 by the authors. Licensee MDPI, Basel, Switzerland. This article is an open access article distributed under the terms and conditions of the Creative Commons Attribution (CC BY) license (<https://creativecommons.org/licenses/by/4.0/>).

1. Introduction

In the construction industry, slabs play a significant role as an essential structural component, providing space for buildings. Solid slabs, however, are associated with certain drawbacks, including high costs, excessive material usage, low structural efficiency, prolonged construction periods, and environmental pollution. Consequently, hollow slabs are increasingly being adopted as a substitute for reinforced concrete solid slabs. Typically, slabs are designed to withstand vertical loads. Hollow slabs are designed to maximize the efficiency of vertical components like shear walls and columns by minimizing their weight. This is achieved by reducing the amount of steel bars required in their construction. As a result, costs are lowered and construction time is saved [1–3]. Cement, as one of the primary constituents of concrete, emits a substantial amount of carbon dioxide during its manufacturing process, resulting in adverse environmental effects [4,5]. Previous studies have demonstrated that hollow slabs [6–13], when compared to solid slabs of comparable span and strength, can reduce the amount of concrete required by approximately 35%. This reduction in concrete usage not only leads to significant cost savings but also helps mitigate environmental pollution. In a study conducted by Cho et al. [14], it was observed that the production of hollow slabs generates lower CO₂ emissions compared to solid

slabs. However, it is important to consider the CO₂ generated during the production of internal molds for hollow slabs as well. The drawbacks of hollow slabs are also obvious. For traditional hollow slabs, hollow slabs can affect their bending and shear resistance performance [15–21]. Azad et al. [22] conducted experiments to investigate the impact of the hollow ratio on the bending and shear-bearing capacity of hollow slabs. They found that hollow slabs can be effectively utilized in components with low-shear-resistance requirements. Amoushahi et al. [23] conducted an experimental study on the bending and shear-bearing capacity of hollow slabs reinforced with steel cages and wrapped in spherical internal molds. This study revealed that solid and hollow slab specimens exhibited similar failure modes. However, the bending and shear-bearing capacity of hollow slabs were found to be influenced by the presence of steel cages. The shear capacity of hollow slabs was found to be considerably lower than that of solid slabs. Additionally, the different concrete pouring methods were observed to have no impact on the bearing capacity and performance of hollow slabs. Valivonis et al. [24] conducted research on the stamping strength of two-way hollow slabs, focusing on the high-risk region where slab column connections and concentrated loads are applied. The failure of the board may be attributed to punching. This study aims to analyze three different punching areas and to propose a new calculation method for determining the punching capacity of hollow slabs based on Eurocode 2 design code. Chung et al. [19] analyzed the possibility of applying a donut-type two-way voided slab, which was investigated with a 12-point two-way bending test focused on global behaviors. The test results showed that one donut-type two-way voided slab acted like a conventional two-way reinforced concrete slab with the load distributed evenly between the different directions; however, another donut-type two-way voided slab with different characteristics showed an uneven load distribution with different crack patterns. In a study conducted by Chung et al. [25], the bending performance of ordinary hollow slabs was investigated. Six specimens were created and the experimental outcomes demonstrated that the bending performance of hollow slabs, when they reached the limit state, was comparable to that of traditional solid slabs. Additionally, it was discovered that the current design specifications for concrete solid slabs were suitable for application to hollow slabs.

Currently, scholars are opting for Glass-Fiber-Reinforced Polymer (GFRP) to increase the strength of hollow internal molds and enhance the performance of hollow components. Fiber-Reinforced Polymer (FRP) encompasses various materials such as Carbon-Fiber-Reinforced Polymer (CFRP), Basalt-Fiber-Reinforced Polymer (BFRP), and Glass-Fiber-Reinforced Polymer (GFRP). In general, CFRP has higher mechanical properties and excellent fatigue resistance, corrosion resistance, and creep resistance. However, the high price of carbon fiber and the low elongation at break are the two main pain points in engineering application. In contrast, GFRP and BFRP composites have abundant material sources, mature preparation technology, reasonable price, and high elongation at break, which make its application in engineering more acceptable. On the other hand, the resin matrix, an essential component of B/GFRP, will react with free OH[−] ions in an alkaline environment and hydrolyze, thus accelerating the water molecules in the solution in entering the matrix through osmosis and damaging the interface bonding system between the fiber and the matrix, which also needs to be considered in engineering application [26–29]. GFRP is employed in the reinforcement of hollow slabs to enhance their bending and shear properties. This material surpasses earlier materials in terms of strength, stiffness, and corrosion resistance, and additionally offers the advantages of being lightweight, being easy to install on site, and possessing long-term durability. The application of FRP materials in the civil engineering industry is relatively slow. Many scholars are striving for it, such as Nguyen et al. [30] who conducted failure mold tests on hollow slabs made of FRP material. The results show that FRP material improves the shear resistance of hollow slabs and can withstand greater loads than ordinary hollow slabs. Chung et al. [31] investigated the flexural strength, stiffness, and deflection of donut-type voided slabs using the void shape and void shaper fixing method as variables. The test results showed that the bending

strength of the donut-type void plate was equivalent to 98% and 105% of that of the solid RC specimens and that the donut-type void plate specimens had sufficient bending ductility. The stiffness was increased by 7% compared to the non-donut-shaped hollow-core panels. Kang et al. [15] analyzed the shear behavior of biaxial hollow slabs using nonlinear FEM according to various design parameters such as concrete strength, reinforcement ratio, the diameter and spacing of void spheres, and the shear-span-to-depth ratio. Tynski et al. [32] conducted a study to investigate the suitability of hollow structures made from Glass-Fiber-Reinforced Polymer (GFRP) for bridge decks. In their experimental setup, they produced a total of 18 specimens and assessed the impact of incorporating GFRP material on the stiffness of concrete. The results demonstrated that the addition of GFRP resulted in an increase in concrete stiffness ranging from 62% to 78%. These findings present promising prospects for the application of GFRP in bridge deck construction. Al-Fakher et al. [33] studied a composite reinforcement system (CRS) to improve the connection performance between GFRP materials and concrete, and the results showed that the bearing capacity and initial stiffness of GFRP circular tubular internal mold hollow slabs under this system were increased by 112% and 24%, respectively. Wu et al. [34] found that increasing the length of the first and second layers of FRP reinforcement zones from 300 mm to 450 mm had almost no effect on the shear strength of medium- and low-prestressed hollow slabs. However, extending the reinforcement area to 600 mm significantly increased the shear strength by 26–45%.

As a new type of non-core-forming perforating component, the application of GFRP high-strength thin-walled inner molds simplifies the construction process of hollow structures while potentially participating in structural load bearing. This article focuses on the impact of GFRP high-strength thin-walled inner molds on the load-bearing performance of structures. Initially, the load-bearing capacity of hollow slabs that considers the participation of GFRP high-strength thin-walled inner molds in load bearing is analyzed. Based on this, the bending moment adjustment performance of continuous hollow slabs with GFRP high-strength thin-walled inner molds is further studied. Lastly, this study extends to the floor slabs in actual engineering projects, examining the similarities and differences in the load-bearing performance between GFRP high-strength thin-walled inner-mold hollow floor slabs and similar dense ribbed floor slabs. The research results will provide a theoretical basis for the design and application of GFRP high-strength thin-walled inner molds.

2. Specimen Preparation and Experimental Test Methods

2.1. Experiments of GFRP on the Bearing Capacity and Moment Modification Limitation of Hollow Continuous Slab Sections

The load-bearing performance of structures can be influenced by the use of GFRP high-strength thin-walled internal molds, due to their own strength and stiffness. In this study, the cross-sectional bearing capacity of GFRP high-strength thin-walled circular hollow slabs was determined through experimental testing. The actual stress state of GFRP internal molds was considered in calculating and analyzing the cross-sectional bearing capacity. The experimental results were used to analyze and discuss the issue of bending moment modification.

(1) Experiments of GFRP on the Bearing Capacity of Hollow Continuous slab Sections

This article conducted static load tests on four double-span circular hollow continuous slabs. The calculated span of the specimen was 3200 mm, the slab thickness was 160 mm, the height-to-span ratio was $h/l = 1/20$, and the slab width was 600 mm. There were 48 GFRP high-strength thin-walled pipes (with a length of 470 mm, a diameter of 100 mm, and a wall thickness of 5 mm), with a hollow ratio of 28%. The detailed arrangement is shown in Figure 1. Four continuous slabs were used with different amounts of negative and positive bending moment reinforcements, as shown in Table 1. The loading method of the experiment involved symmetrically applying a concentrated load on each mid-span. The bending moments of the intermediate support section and the mid-span section under

different load levels can be calculated by using the measured reaction forces and load values at the intermediate support. By varying the ratio of the negative bending moment to the positive bending moment around 24 kN, various values for the amplitude modulation of the bending moment can be obtained.

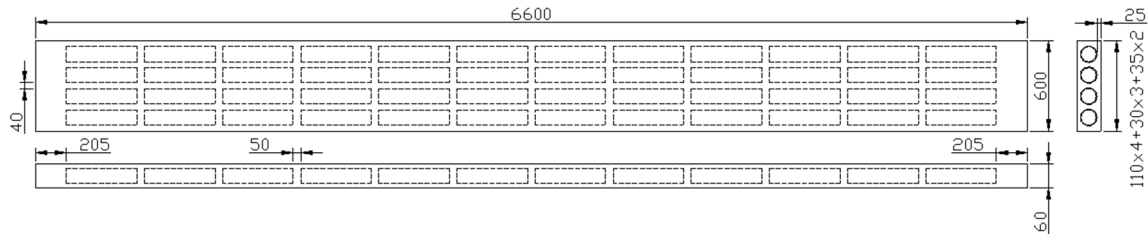


Figure 1. Construction of the continuous slab.

Table 1. Basic parameters of test pieces.

Specimen Number	JLB-1	JLB-2	JLB-3	JLB-4
Negative	5 φ 8	2 φ 8 + 4 φ 6	5 φ 8	2 φ 8 + 3 φ 6
Positive	3 φ 8 + 2 φ 10	6 φ 8	5 φ 8 + 1 φ 6	3 φ 8 + 2 φ 10
AMF	19.3%	25.3%	16.5%	30.7%

Four continuous slabs were used with different amounts of negative and positive bending moment reinforcements, as shown in Table 1. In Table 1, Negative refers to a negative moment longitudinal reinforcement, Positive refers to a positive moment longitudinal reinforcement, and AMF refers to the amplitude modulation factor.

(2) Experiments of GFRP on the Moment Modification Limitation of Hollow Continuous slab Sections

In order to further make the use of GFRP circular tubular hollow slabs more economic and effective in engineering structures, the situation of its bending moment modification was studied and analyzed in this article.

The test was performed by graded loading with jacks, and a concentrated load was applied in the middle of each span (Figures 2 and 3). After each load stabilization, the middle support reaction force, steel and concrete strain, middle support section corner and crack, and deflection were measured. In the test, in order to measure the length of the plastic hinge zone when a plastic hinge is formed in the center support section, the outer reinforcement patch method was used, i.e., the outer surface of the reinforcement was polished and pasted with reinforcement strain gauges along the longitudinal direction in the longer range on both sides of the center support section, and then coated with an epoxy resin to protect it (Figure 4).

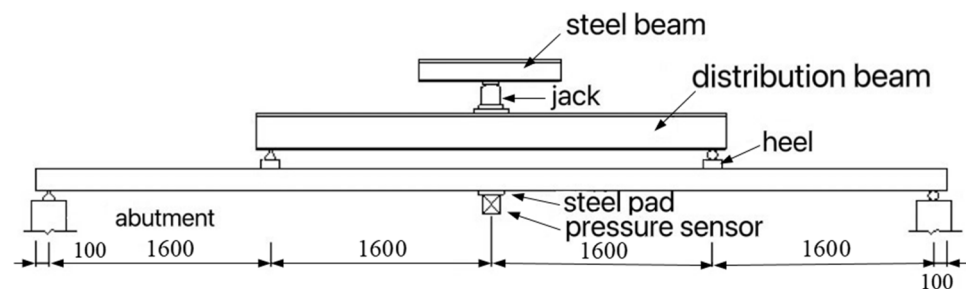


Figure 2. Loading system.



Figure 3. Loading system of the continuous hinge.



Figure 4. Strain gauge of steel in plastic slab.

2.2. Experiments on the Force Performance of GFRP High-Strength Thin-Walled Internal Mold Honeycomb Core Slab

In addition to GFRP circular tubular hollow internal mold slabs, there is also a GFRP honeycomb core slab. There is relatively little research on this structural system both domestically and internationally. Based on this situation, experimental comparative studies have been conducted on honeycomb core slabs and waffle slabs.

(1) Test purpose and test piece production

The internal force, deformation, cracks, strain distribution of concrete and reinforcement, and damage morphology of the slab were measured by testing the honeycomb core slab under various levels of loading. The contribution of the core mold to the stiffness of the honeycomb core slab and its impact on the basic mechanical properties of the honeycomb core were studied by comparing the honeycomb core slab with the waffle slab; the bonding performance of the honeycomb core internal mold with concrete during loading was studied.

The plane size of the honeycomb core slab was 4250×4250 , the size of honeycomb core internal molds was $350 \times 350 \times 130$, the thickness of the internal mold base plate was 15 mm, the other wall thickness was 7 mm, the width of the cast-in-place concrete rib of slab was 50 mm, the hollow rate was 42%, and the four-sided solid support was adopted. The mold was made indoors, cast-in-place with C25 commercial concrete, and naturally maintained indoors for 28 d.

The design load value of the honeycomb core slab was 6.87 kN/m^2 , and the two-way slab with four sides embedded was designed with reinforcement according to the current code. The structure and geometry of the honeycomb core slab are shown in Figure 5, the reinforcement is shown in Figure 6, and the photo before casting is shown in Figure 7.

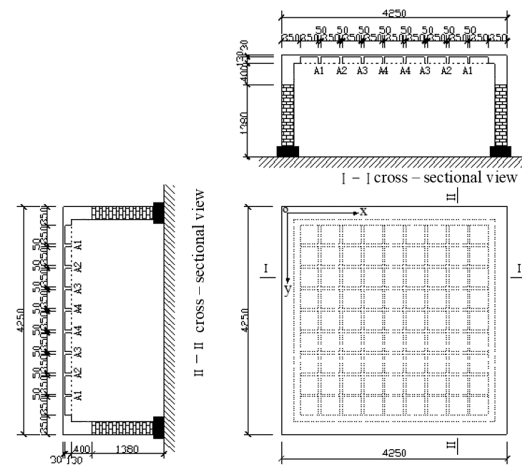


Figure 5. Plan and section of honeycomb core slab and waffle slab.

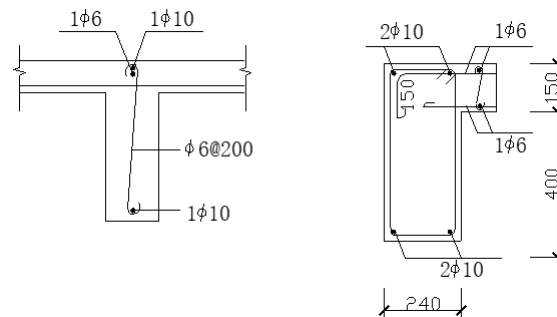


Figure 6. Transverse reinforcement diagram of ribs and beams.

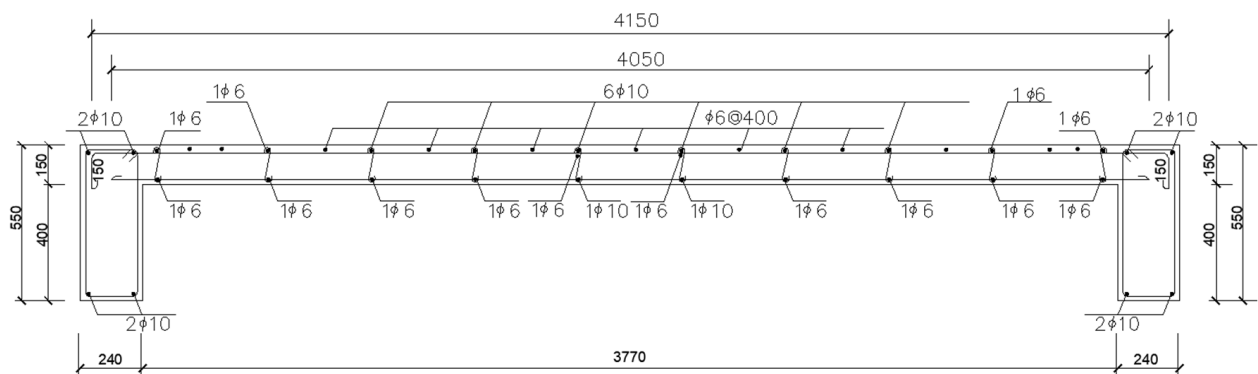


Figure 7. Longitudinal reinforcement diagram of ribs.

The dimensions, support conditions, concrete strength grade, and reinforcement of the test waffle slab were the same as those of the honeycomb core slab. Meanwhile, in order to make the internal structure of the waffle slab the same as that of the honeycomb core slab, the internal foam ($350 \times 350 \times 130$) with the same size as the internal mold of the honeycomb core was used as the filling block of the waffle slab. The structure and geometry of the waffle slab are shown in Figure 5.

(2) Test method

The test is a destructive static test in which a uniform load is applied to the test slab in a graded manner. The experimental device and loading method are shown in Figures 8 and 9. Steel strain gauges were set in the middle and span end of each concrete rib of the slab, and concrete strain gauges were pasted at the center, $1/4$ span, and $1/8$ span of the concrete on the surface of the slab to record the strain condition at the key points of the

slab. A percentage meter was set at the center and 1/4 span of the slab to measure its deformation. In order to measure the real deformation value of the slab, a percentage meter was also set at the center of the wall to measure the settlement of the foundation and the compression of the wall as the settlement value of the support of the slab. The test loading was divided into 11 levels (Table 2), the load was held for 10–20 min after each level of loading, after the deformation of the slab and the crack stabilization, and then the crack development was observed and the deflection and strain values of each measurement point were read.

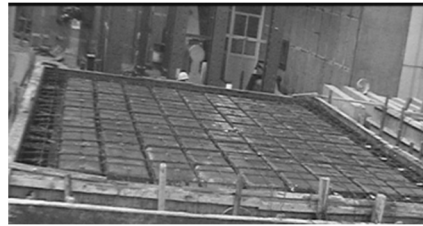


Figure 8. Honeycomb core slab before pouring concrete.



Figure 9. Loading of honeycomb core slab.

Table 2. Slab loading classification table (kN/m²).

Level	1	2	3	4	5	6	7	8	9	10	11
Current level load	2.34	4.16	4.16	4.16	4.16	3.05	3.05	3.05	2.44	2.44	2.34
Accumulated load	2.34	6.51	10.68	14.85	19.01	22.06	25.11	28.16	30.59	33.03	35.37

3. Theoretical Analysis

3.1. Analysis of Section Flexural-Load-Bearing Capacity of GFRP Circular Tubular Hollow Slab

The measured failure load and control section internal force values under the failure load of each continuous slab are shown in Table 3.

Table 3. Theoretical values and measured values of normal section bearing capacity.

Specimen Number	P'_u	M'_{bu}	M'_{lu}	M_{bu}	M_{lu}
JLB-1	24.5	13.655	14.647	9.240	11.478
JLB-2	24.65	13.391	14.899	8.531	11.074
JLB-3	23.75	13.751	14.005	9.24	10.522
JLB-4	23.65	11.734	14.835	7.435	11.478

Note: (1) The unit of force is kN, the unit of bending moment is kN·m. (2) P'_u is the measured value of the failure load; M'_{bu} is the measured value of the ultimate bending moment of the middle support section; M'_{lu} is the measured ultimate bending moment in the span section. M_{bu} and M_{lu} are the corresponding theoretical values.

In Table 3, the theoretical values of the flexural bearing capacity of the mid-support section and mid-span section are calculated based on the cross-section of ordinary reinforced concrete hollow slabs. From the table, it can be observed that the measured ultimate bending moment values of the cross-section exceed the theoretical values calculated for ordinary reinforced concrete hollow slabs. This suggests that GFRP pipes may contribute to

the structural stress and enhance the cross-section's bearing capacity. According to relevant experimental research [35], GFRP pipes have a tensile strength of up to 42 MPa, which is much greater than the tensile strength of concrete. Therefore, the influence of GFRP pipes is not considered in the calculation, which will differ from the actual situation.

- (1) Basic assumptions for calculation
 - (1) Plane section assumption.
 - (2) Neglect of the effect of concrete in the tensile zone.
 - (3) Materials' constitutive relationships are as below.
 - (i) The stress–strain relationship of concrete under compression. The typical stress–strain curve of concrete used for section strength calculation in the European Concrete Association's standard specification (CEB-FIP Models Code) (Figure 10) is taken.
 - (ii) The stress–strain curve of the steel reinforcement adopts a simplified ideal elastic–plastic stress–strain relationship (Figure 11).
 - (iii) The tensile stress–strain relationship of pipes. This study conducted tensile tests on sliced pipe strips [36,37], using the stress–strain relationship of the pipe provided by it (Figure 12), where the ultimate tensile strength $f_t = 42$ MPa, $k\varepsilon_0 = 0.002$, ultimate tensile strain $\varepsilon_{tu} = 0.006$, and elastic modulus $E_t = 2 \times 10^4$ Mpa.
- (2) Stress Analysis and Bearing Capacity Calculation of GFRP Pipe Section (Case I)

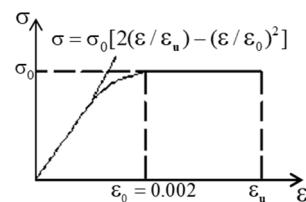


Figure 10. Stress–strain curve of concrete.

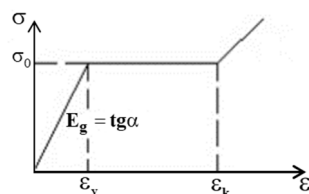


Figure 11. Stress–strain curve of steel.

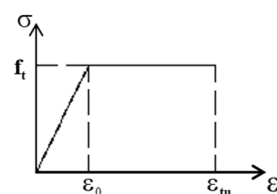


Figure 12. Stress–strain curve of pipe.

Figure 13a shows a section of a hollow slab with a GFRP tube placed in the center. This study analyzes a more general case where the stress state of the GFRP tube cross-section is divided into three parts: one part was cracked and stopped functioning, one part of the stress remains unchanged at the ultimate strength, and another part of the stress changes linearly along the height of the section (this situation is referred to as Case I in this article).

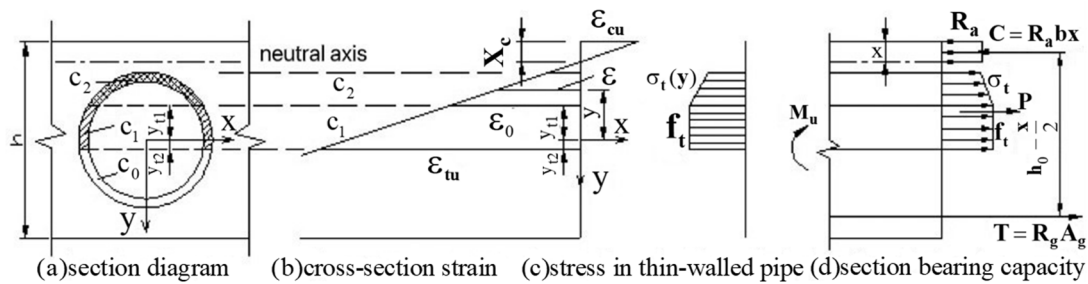


Figure 13. Stress analysis of the slab section.

According to the assumption of a flat section, the strain distribution on the slab section during failure is shown in Figure 13b. The stress distribution on the section of the GFRP pipe can be obtained from the stress–strain relationship of the tube, as shown in Figure 13c. The C_0 section of the thin-walled tube ruptured due to the strain exceeding its ultimate tensile strain, the stress in the C_1 section remained at its ultimate tensile strength f_t , and the stress in the C_2 section was distributed linearly along the height of the section.

Establishing a coordinate system as shown in Figure 13a, and calculating the strain at any height of the C_2 section of the tube ε , the corresponding relationship of coordinate y corresponding to this height is

$$\varepsilon = \left(\frac{h}{2} - x_c + y \right) \frac{\varepsilon_{cu}}{x_c} \quad (1)$$

Stress–strain relationship of pipes:

$$\sigma_t(\varepsilon) = E_t \varepsilon \quad (2)$$

From the above two formulas, the relationship between the wall stress σ_t of part C_2 and the section height y can be obtained:

$$\sigma_t(y) = E_t \left(\frac{h}{2} - x_c + y \right) \frac{\varepsilon_{cu}}{x_c} \quad (3)$$

The calculation formula of the slab section bearing capacity is shown in Figure 13d. If the sum of horizontal internal forces on the section is zero, then $T + P + C = 0$. T is the combined tensile stress of reinforcement, C is the combined compressive stress of concrete, and P is the combined stress of the pipe wall. As shown in Figure 14, if the microsection d_y is taken in the horizontal direction, the resultant stress P of the pipe wall of C_1 and C_2 parts can be obtained by integration as

$$P = n \left(\int_{y_{t1}}^{y_{t2}} f_t \cdot 2\sqrt{R^2 - y^2} dy - \int_{y_{t1}}^{y_{t2}} f_t \cdot 2\sqrt{R^2 - y^2} dy \right) + n \left[\int_{-R}^{y_{t1}} \sigma_t(y) \cdot 2\sqrt{R^2 - y^2} dy \right] \quad (4)$$

$$R_a b x = R_g A_g + n \left(\int_{y_{t1}}^{y_{t2}} f_t \cdot 2\sqrt{R^2 - y^2} dy - \int_{y_{t1}}^{y_{t2}} f_t \cdot 2\sqrt{R^2 - y^2} dy \right) + n \left[\int_{-R}^{y_{t1}} \sigma_t(y) \cdot 2\sqrt{R^2 - y^2} dy \right] \quad (5)$$

where the integral limits y_{t1} and y_{t2} are functions of the height of the equivalent concrete pressured region (the calculation process can be derived from Figure 13b).

$$y_{t1} = \frac{\varepsilon_0}{\varepsilon_{cu}} \cdot \frac{x}{0.8095} - \frac{h}{2} + \frac{x}{0.8095} \quad (6)$$

$$y_{t2} = \frac{\varepsilon_{tu}}{\varepsilon_{cu}} \cdot \frac{x}{0.8095} - \frac{h}{2} + \frac{x}{0.8095} \quad (7)$$

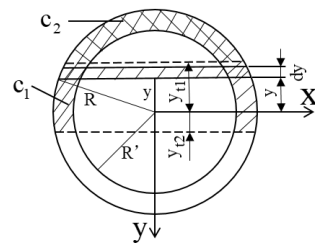


Figure 14. Selection of integral micro-segment of pipe.

The moment is taken at the point of action of the resultant forces on the concrete compression zone.

$$M_u = R_g A_g \left(h_0 - \frac{x}{2} \right) + n \left[\int_{y_{t2}}^{y_{t1}} f_t \cdot 2\sqrt{R^2 - y^2} dy \cdot \left(\frac{h}{2} - \frac{x}{2} + y \right) - \int_{y_{t1}}^{y_{t2}} f_t \cdot 2\sqrt{R'^2 - y^2} dy \cdot \left(\frac{h}{2} - \frac{x}{2} + y \right) \right] + n \left[\int_{-R}^{y_{t1}} \sigma_t(y) \cdot 2\sqrt{R^2 - y^2} dy \cdot \left(\frac{h}{2} - \frac{x}{2} + y \right) - \int_{-R'}^{y_{t1}} \sigma_t(y) \cdot 2\sqrt{R'^2 - y^2} dy \cdot \left(\frac{h}{2} - \frac{x}{2} + y \right) \right] \quad (8)$$

where M_u is the ultimate flexural load capacity of the slab section; n is the number of thin-walled tubes; R_g , A_g are the tensile strength of reinforcing steel, the axial-compressive strength of concrete, and the area of reinforcing steel; h_0 and h are the effective height of a cross-section and the actual height of a cross-section; x is the height of the concrete-equivalent pressure zone; actual pressure zone height $x_c = x/0.8095$; R is the outer and inner radius of thin-walled tubes; f_t and E_t are the ultimate tensile strength of the pipe and modulus of elasticity of the pipe; $\sigma_t(y)$ is the stress distribution function of the C_2 part of the thin-walled tube, calculated by Equation (3); the ultimate compressive strain of concrete can be taken as 0.003 according to the specification; ϵ_0 is the strain at which the tube just reaches its tensile ultimate strength, which is 0.002; and ϵ_{tu} is the ultimate tensile strain of the tube, which is 0.006.

Equations (4) and (8) are the basic formulas for calculating the cross-sectional bearing capacity of GFRP circular hollow slabs. Firstly, the height x of the equivalent compression zone of concrete is solved from Equation (4), and then the flexural bearing capacity of the section is found by substituting into Equation (8). Since the role of GFRP pipes is considered, the solution process is quite complicated and difficult to solve for the height x of the concrete-equivalent pressure zone, so the only way to calculate the bearing capacity of the cross-section by Equations (4) and (8) is to use numerical analysis. The conditions for the application of the above formula are discussed below. Based on the above calculation process, it is known that the integration limits y_{t1} and y_{t2} should satisfy the following conditions:

$$-R' \leq y_{t1} \leq R' \quad (9)$$

$$-R' \leq y_{t2} \leq R' \quad (10)$$

Bringing Equations (6) and (7) into Equations (9) and (10), respectively:

$$\begin{cases} \frac{0.8095\epsilon_{cu}}{\epsilon_0 + \epsilon_{cu}} \left(-R' + \frac{h}{2} \right) \leq x \leq \frac{0.8095\epsilon_{cu}}{\epsilon_0 + \epsilon_{cu}} \left(R' + \frac{h}{2} \right) \\ \frac{0.8095\epsilon_{cu}}{\epsilon_{tu} + \epsilon_{cu}} \left(-R' + \frac{h}{2} \right) \leq x \leq \frac{0.8095\epsilon_{cu}}{\epsilon_{tu} + \epsilon_{cu}} \left(R' + \frac{h}{2} \right) \end{cases} \quad (11)$$

(3) Stress Analysis and Bearing Capacity Calculation of GFRP Pipe Section (Case II)

When the height x of the concrete pressure zone is relatively small, it will produce a situation where the stress condition of the GFRP pipe section is divided into only two parts: one part was cracked and stopped functioning, and the stress of the other part fully reached the ultimate strength. As shown in Figure 15, the C_0 part of the thin-walled tube cracked and stopped functioning, and the stress in the C_1 part was maintained at its ultimate tensile strength f_t (this case is referred to as Case II in this paper).

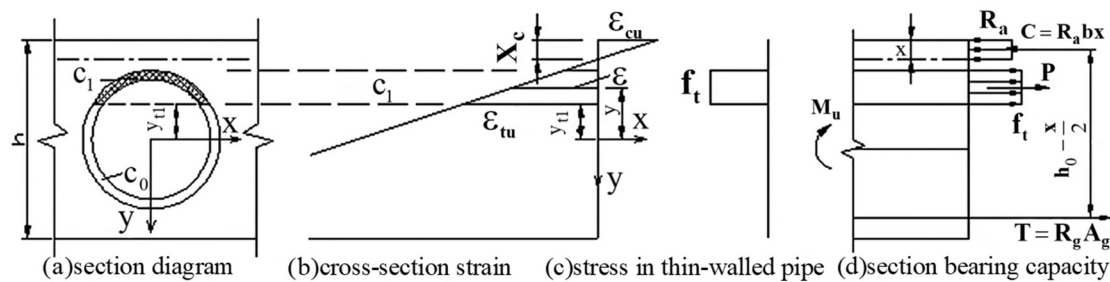


Figure 15. Stress analysis of the slab section.

The integral micro-segment can still be selected according to Figure 14, and the combined stress P at the pipe wall in part C_1 is obtained by integration as

$$P = n \left(\int_{-R}^{y_{t2}} f_t \cdot 2\sqrt{R^2 - y^2} dy - \int_{-R'}^{y_{t2}} f_t \cdot 2\sqrt{R'^2 - y^2} dy \right) \quad (12)$$

Since $T + P + C = 0$, it follows that

$$R_a b x = n \left(\int_{-R}^{y_{t2}} f_t \cdot 2\sqrt{R^2 - y^2} dy - \int_{-R'}^{y_{t2}} f_t \cdot 2\sqrt{R'^2 - y^2} dy \right) \quad (13)$$

where the integral limit y_{t2} is

$$y_{t2} = \frac{\varepsilon_{tu}}{\varepsilon_{cu}} \cdot \frac{x}{0.8095} - \frac{h}{2} + \frac{x}{0.8095} \quad (14)$$

Then, take the moment at the point of action of the combined force C on the concrete in the pressure zone:

$$M_u = R_g A_g \left(h_0 - \frac{x}{2} \right) + n \left[\int_{-R}^{y_{t2}} f_t \cdot 2\sqrt{R^2 - y^2} dy \cdot \left(\frac{h}{2} - \frac{x}{2} + y \right) - \int_{-R'}^{y_{t2}} f_t \cdot 2\sqrt{R'^2 - y^2} dy \cdot \left(\frac{h}{2} - \frac{x}{2} + y \right) \right] \quad (15)$$

Firstly, the concrete-equivalent compression zone height x is solved by Formula (13), and then the section flexural bearing capacity is found by substituting into Formula (15). In the case discussed in this section, the conditions of application of the basic formula are

$$-R' \leq y_{t2} \leq R \quad (16)$$

$$x \leq \frac{0.8095\varepsilon_{cu}}{\varepsilon_0 + \varepsilon_{cu}} \left(-R + \frac{h}{2} \right) \quad (17)$$

Combining the two equations yields

$$\frac{0.8095\varepsilon_{cu}}{\varepsilon_{tu} + \varepsilon_{cu}} \left(-R' + \frac{h}{2} \right) \leq x \leq \frac{0.8095\varepsilon_{cu}}{\varepsilon_0 + \varepsilon_{cu}} \left(-R + \frac{h}{2} \right) \quad (18)$$

Equation (18) for the thin-walled tube cross-sectional force conditions only produce two different parts (case II), and the height of the concrete pressure zone x should be satisfied by the preconditions.

If the actual height of the pressure zone is less than the value of the left side of Equation (18), then the solution using Equation (13) is no real solution; the actual situation is where the entire thin-walled tube section has been completely cracked and has stopped functioning. If the actual height of the pressure zone is greater than the value on the right side of Equation (18), then the solution from Equation (13) is incorrect and should be calculated according to the situation in case I.

Finally, a question needs to be solved. When the reinforcement area is large (such as $A_g = 370 \text{ mm}^2$), there are answers using the formulas for both case I and case II. For case I, substituting the relevant parameters into Equation (11) yields $15.5 \leq x \leq 40.2$. For case II,

substituting the relevant parameters into Equation (18) yields $8.95 \leq x \leq 40.2$. From the above two inequalities, it can be seen in the $15.5 \leq x \leq 40.2$ part that they are overlapping, so when the reinforcement area is large, case I and case II of the bearing capacity calculation have solutions.

According to the above, the height of the concrete pressure zone in case I is larger than the height of the concrete pressure zone in case II. The reinforcement rate is the main factor affecting the height of the concrete pressure zone. There should exist a critical reinforcement area, which should be calculated according to Case I when the reinforcement amount is lower, and according to Case II, when the reinforcement amount is greater. This critical reinforcement area can be calculated by the program. The critical reinforcement area at this point can be calculated to be 360 mm^2 .

3.2. GFRP Hollow-Continuous-Slab Bending Moment Modification Limit Analysis

(1) Ultimate plastic rotation capacity of the middle support section

In the experiments, the middle support section of each continuous slab has sufficient rotational force after the formation of a plastic hinge to make the structure reach the complete internal force redistribution. When the structure reaches the ultimate load damage, the plastic hinge of the middle support section still has the remaining rotational capacity, which has not been fully exerted, so only the ultimate rotational capacity $[\theta_p]$ of the plate section is theoretically calculated.

The ultimate plastic rotation capacity $[\theta_p]$ of the cross-section can be calculated by the following formula:

$$[\theta_p] = \int \phi_i dx = (\phi_u - \phi_y) l_p \quad (19)$$

where ϕ_i is the plastic curvature distribution function of the component; ϕ_u is the section curvature when the cross-sectional bending moment $-u$ reaches its ultimate bending moment; ϕ_y is the cross-sectional curvature at the start of yielding of the tensile reinforcement; and l_p is the length of the plastic hinge zone for the Sakashino formula [38]: $l_p = 2 \left(1 - 0.5 \mu \frac{R_s}{R_a} \right) h_0$.

According to the assumption of the flat section, the ultimate curvature ϕ_u and yield curvature ϕ_y of the member are found and substituted into Equation (19) to obtain

$$[\theta_p] = (\phi_u - \phi_y) l_p = \left[\frac{\varepsilon_{cu}}{\xi_c h_0} - \frac{\varepsilon_{gy}}{(1 - \xi_y) \cdot h_0} \right] \cdot l_p \quad (20)$$

where ε_{cu} is the ultimate compressive strain of concrete and, according to the specification, is taken as a constant value of 0.003 [39]; ξ_c is the height factor of the concrete pressure zone at the time of cross-sectional damage; ε_{gy} is the strain at initial yield of the tensile reinforcement, which can be approximated as $\varepsilon_{gy} = R_g / E_g$; and ξ_y is the height factor of the relative compression zone at the initial yield of the tensile reinforcement and can be calculated according to the following formula [40]:

$$\xi_y = \sqrt{[\mu'(n-1) + n\mu]^2 + 2[n\mu + \mu'(1 - \eta_g)(n-1)]} - [\mu'(n-1) + n\mu] \quad (21)$$

where $n = \frac{E_g}{E_c}$ is the ratio of the reinforcing steel spring form to concrete spring form, and η_g is the cross-sectional internal force arm factor. When compressive reinforcement is not considered, Equation (21) simplifies to

$$\xi_y = \sqrt{n^2 \mu^2 + 2n\mu} - n\mu \quad (22)$$

(2) The plastic angle required for bending moment modification

1. Experimental measurement results

The experiment used the CQJ-RS-S1 multifunctional electronic digital display inclinometer to measure the rotation of the center support section. This study is concerned with the plastic corner, and the measured values include the elastic part of the corner, so the elastic corner needs to be deducted. The following approach is used to find θ_e : based on the measured deflection $f_{l/4}$ of the 1/4 span section near the middle support under yielding load, the angle of rotation θ_e is found from the geometric relationship (Figure 16).

$$\theta_e = 2 \arctan \frac{f_{l/4}}{800} \quad (23)$$

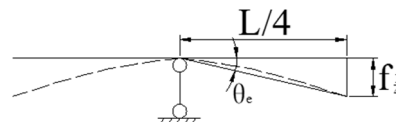


Figure 16. Elastic corner calculation.

In fact, the result calculated by Equation (23) is on the small side, because the curvature of the elastic phase member is very small, and the calculation error is also very small and fully satisfies the accuracy requirement. After finding θ_e , the plastic rotation angle $\theta_p = \theta_{\text{Measure}} - \theta_e$ can be found, and the results are shown in Table 4.

Table 4. Theoretical values and measured values of plastic turn angle required by moment modification.

Specimen Number	JLB-1	JLB-2	JLB-3	JLB-4
Measured corner	26.0'	36.6'	19.4'	42.3'
Calculate corner	25.6'	30.5'	21.1'	49'
Error	1.5%	16.7%	8.8%	15.8%

2. Theoretical calculation of the plastic angle required for bending moment modification

In this test, the two-span continuous slab was stressed in a manner (Figure 17) where the plastic hinge appears first in the mid-support section. The energy method was used to find the plastic hinge angle required for bending moment modification.

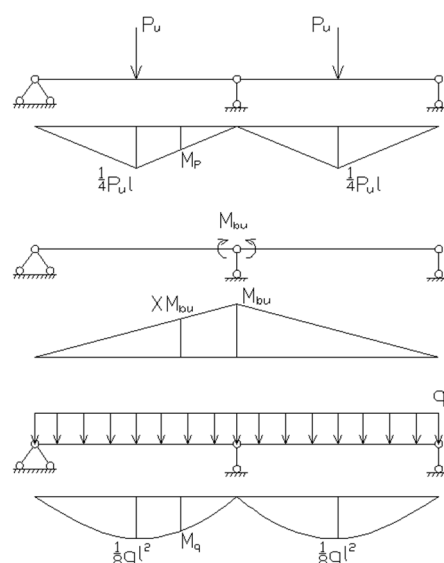


Figure 17. Moment induced by P_u , M_{bu} , and q .

Considering the effects of external load P_u , external force couple M_{bu} , and self-weight q , the resulting bending moment diagram is shown in Figure 17. In the figure, M_p is the

bending moment at any point of the continuous plate under the action of P_u , X is the bending moment at any point when $M_{bu} = 1$, and M_q is the bending moment at any point of the continuous slab under the action of the self-weight q . Define the bending moment of the lower part of the slab under tension as positive. At this point, the bending moment at any point in the slab can be expressed as $M = M_P + XM_{bu} + M_q$.

Assuming that the member between the plastic hinge and the side support works in elasticity, the elastic strain in the slab can be

$$U = \int \frac{M^2}{2EI} dx = \int_0^{2l} \frac{(M_P + XM_{bu} + M_q)^2}{2EI} dx \quad (24)$$

where dx is the length micro-segment of the member. Find the frictionless hinge turning angle caused by the elastic deformation of the member between the middle support hinge and the side support. The load corresponding to this frictionless hinge angle is the external force couple M_{bu} , so the angle can be obtained as

$$-\theta_p = \frac{\partial U}{\partial M_{bu}} \quad (25)$$

where the negative sign in front of θ_p indicates that the direction of rotation of the hinge is opposite to the direction of action of the force couple M_{bu} . Expanding Equation (24) yields

$$U = \int_0^{2l} \frac{M_P^2}{2EI} dx + M_{bu}^2 \int_0^{2l} \frac{X^2}{2EI} dx + \int_0^{2l} \frac{M_q^2}{2EI} dx + \int_0^{2l} \frac{M_P M_q}{EI} dx + M_{bu} \int_0^{2l} \frac{M_P X}{EI} dx + M_{bu} \int_0^{2l} \frac{M_q X}{EI} dx \quad (26)$$

According to Equation (25), the partial derivative of M_{bu} for Equation (26) is obtained.

$$-\theta_p = \frac{\partial U}{\partial M_{bu}} = \int \frac{M_P X}{EI} dx + M_{bu} \int \frac{X^2}{EI} dx + \int \frac{M_q X}{EI} dx \quad (27)$$

Integrating Equation (27), the frictionless hinge angle caused by the elastic deformation of the member between the middle support hinge and the side support is

$$\theta_p = \frac{l}{EI} \left(\frac{P_u l}{8} + \frac{ql^2}{12} - \frac{2M_{bu}}{3} \right) \quad (28)$$

Equation (28) is the calculation of the plastic angle required for amplitude adjustment.

3. Meet the load-bearing capacity requirements of the bending moment modification limit

Combined with the tests performed, it is clear that the problem to be solved is as follows: the cross-sectional form and span diameter of the two-span continuous slab are known, the material properties of the reinforcement and concrete are used, and given the external load P_u , the value of the bending moment modification $[\beta]$ that can withstand P_u is solved.

Under the bending moment modification β , the bearing capacity of the middle support section M_{bu} is

$$M_{bu} = (1 - \beta) \frac{3}{16} P_u l$$

Substituting the above equation into Equation (28):

$$\theta_p = \frac{l}{EI} \left(\frac{P_u l}{8} + \frac{ql^2}{12} - \frac{2M_{bu}}{3} \right) = \frac{P_u l^2}{8EI} \beta + \frac{ql^3}{12EI} \quad (29)$$

In the case where the plastic rotation of the middle support section is fully utilized, the plastic angle of the section required to complete the modification is equal to the plastic angle of the section that can be provided by the section $\theta_p = [\theta_p]$, so from Equations (29) and (30):

$$\frac{P_u l^2}{8EI} \beta + \frac{q l^3}{12EI} = \left[\frac{\varepsilon_{cu}}{\xi_c h_0} - \frac{\varepsilon_{gy}}{(1 - \xi_y) h_0} \right] \cdot l_p \quad (30)$$

Substituting the Sakashino formula into Equation (30), we can show that

$$\beta = \left(\frac{0.8095 \varepsilon_{cu}}{\mu \frac{R_g}{R_a}} - \frac{\frac{R_g}{E_g}}{1 - \sqrt{\mu^2 n^2 + 2\mu n} + \mu n} \right) \left(2 - \mu \frac{R_g}{R_a} \right) \frac{8EI}{P_u l^2} - \frac{2ql}{3P_u} \quad (31)$$

According to the bending moment–curvature curve of the circular tubular hollow slab section that can be adopted as the principal structure molds of the bifurcation line [41], the bending stiffness EI in the above equation can be approximated as

$$EI = \frac{M_{bu}}{\phi_y} \quad (32)$$

Substituting this into Equation (37) shows that

$$\beta = [\beta] = \left(\frac{0.8095 \varepsilon_{cu}}{\mu \frac{R_g}{R_a}} \frac{1 - \sqrt{\mu^2 n^2 + 2\mu n} + \mu n}{\frac{R_g}{E_g}} - 1 \right) \left(2 - \mu \frac{R_g}{R_a} \right) \frac{8h_0}{P_u l^2} \cdot R_g b h_0 \mu \left(h_0 - \frac{R_g b h_0 \mu}{2R_a b'_i} \right) - \frac{2ql}{3P_u} \quad (33)$$

where b is the equivalent T-section rib width of the plate section, b'_i is the calculated width of the equivalent T-section flange plate, and μ is the reinforcement rate of the center support section.

In order to find the reinforcement ratio μ for the middle support section, the following β will be transformed into an expression for μ .

The elastic bending moment M_e of the middle support section considering the self-weight is

$$M_e = \frac{q l^2}{8} + \frac{3}{16} P_u l \quad (34)$$

Substituting Equation (34) into the defining equation of the bending moment modification factor gives

$$\beta = 1 - \frac{M_a}{M_e} = 1 - \frac{M_{bu}}{\frac{3}{16} P_u l + \frac{1}{8} q l^2} \quad (35)$$

According to the plastic limit analysis method, the relationship between the ultimate bearing capacity of the two-span continuous slab and the section bearing capacity of the control section is found as

$$P_u = \frac{2M_{Bu} + 4M_{lu}}{l} - \frac{ql}{2} \quad (36)$$

where M_{lu} is the bearing capacity of the span section.

Substituting Equation (36) into Equation (35):

$$\beta = 1 - \frac{M_{bu}}{\frac{3}{8} M_{bu} + \frac{3}{4} M_{lu} - \frac{1}{32} q l^2} \quad (37)$$

the term $\frac{1}{32} q l^2$ affected by self-weight is very small, and for the convenience of calculation, it is ignored. Meanwhile, let $k = \frac{M_{lu}}{M_{bu}}$, so the above equation can be expressed as

$$\beta = \frac{6k - 5}{3 + 6k} \quad (38)$$

Denote β as k :

$$k = \frac{5 + 3\beta}{6(1 - \beta)} \quad (39)$$

And then substitute Equation (39) into Equation (36):

$$P_u = \frac{16M_{bu}}{3l(1 - \beta)} - \frac{ql}{2} \quad (40)$$

Solving for β from the above equation yields

$$\beta = 1 - \frac{16M_{bu}}{3l\left(P + \frac{ql}{2}\right)} \quad (41)$$

Substituting Formula (41) into Formula (33):

$$1 - \frac{16R_g b h_0 \mu \left(h_0 - \frac{R_g b h_0 \mu}{2R_a b'_i} \right)}{3l \left(P_u + \frac{ql}{2} \right)} = \left(\frac{0.8095 \epsilon_{cu}}{\mu \frac{R_g}{R_a}} \frac{1 - \sqrt{\mu^2 n^2 + 2\mu n + \mu n}}{\frac{R_g}{E_g}} - 1 \right) \left(2 - \mu \frac{R_g}{R_a} \right) \frac{8h_0}{P_u l^2} \cdot R_g b h_0 \mu \left(h_0 - \frac{R_g b h_0 \mu}{2R_a b'_i} \right) - \frac{2ql}{3P_u} \quad (42)$$

The final result of the above algorithm programmed by computer iterative solution when taking $P_u = 24$ kN is that the bending moment amplitude limit $[\beta]$ for the continuous plate to meet the bearing capacity requirement is 35.65%.

3.3. Comparative Analysis of Theoretical Calculation of Honeycomb Core Slab and Waffle Slab

According to the principle of equivalent bending stiffness, the honeycomb core slab and waffle slab can be equivalent to orthotropic plates, and the internal force and deformation of the floor can be solved by using elastic plate theory.

(1) Stiffness equivalence

For the honeycomb core slab, the cross-section is a multi-chamber structure with denser beam ribs, while the waffle slab cross-section is in the form of multiple T-beam ribs, as shown in Figures 18 and 19.

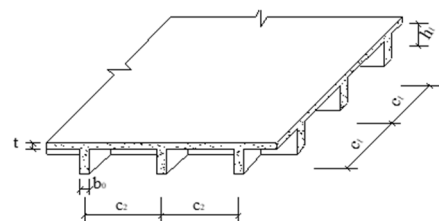


Figure 18. Molds of waffle slab.

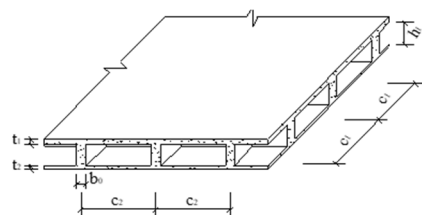


Figure 19. Honeycomb core slab.

The equivalent stiffness of the waffle slab is

$$D_x = \frac{EI_x}{C_1}; D_y = \frac{EI_y}{C_2}; D_1 = \frac{\mu Eh^3}{12(1-\mu^3)}; D_{xy} = \frac{Eh^3}{24(1+\mu)} + \frac{E}{8(1+\mu)} \left(\frac{J_x}{a} + \frac{J_y}{b} \right) \quad (43)$$

J_x and J_y are the torsional moments of inertia of the beam ribs.

The equivalent stiffness of the honeycomb core slab is

$$D_x = \frac{EI_x}{C_1}; D_y = \frac{EI_y}{C_2}; D_1 = \mu \sqrt{D_x D_y}; D_{xy} = \frac{EA^2}{2(1+\mu)w \sum \frac{ds}{t}} \quad (44)$$

where I_x and I_y are the moments of inertia of the entire section to the neutral axis; C_1 and C_2 are the spacing of the beam ribs; $A = dw$ is the area enclosed by the perimeter median; d is the distance from the centerline of the wing plate; w is the distance from the centerline of the outer web; and $\frac{ds}{t}$ is the ratio of the perimeter length to the thickness of the constituent section.

(2) Solution of internal force of slab

The calculation coordinate system is chosen as shown in Figure 5. After equating the slab to an orthogonal anisotropic plate, the deflection and bending moment can be obtained by using elastic thin plate theory. To obtain the internal force of the beam rib before the original equivalence, the bending moment of the plate in the vicinity of the beam rib can be integrated, and the integrated value is the bending moment assumed by the beam. Then, the bending moment of the beam rib in the honeycomb core slab is

$$\overline{M}_x = \int_{y-\frac{c_1}{2}}^{y+\frac{c_1}{2}} M_x dy; \overline{M}_y = \int_{x-\frac{c_1}{2}}^{x+\frac{c_1}{2}} M_y dx \quad (45)$$

The bending moments of the beam ribs in the waffle slab are

$$\overline{M}_x = \int_{y-\frac{\varphi c_1}{2}}^{y+\frac{\varphi c_1}{2}} M_x dy; \overline{M}_y = \int_{x-\frac{\varphi c_1}{2}}^{x+\frac{\varphi c_1}{2}} M_y dx \quad (46)$$

where M_x and M_y are the bending moments per unit width; \overline{M}_x and \overline{M}_y are the actual bending moments in the beam; and φ is the weight factor of the bending stiffness provided by the ribs of the waffle slab beam to the total bending stiffness in that direction.

4. Experimental Results and Discussion

4.1. Theoretical Moment Modification Values and Measured Moment Modification Values of Each Continuous Slab

In the test, the four test continuous slabs achieved complete internal force redistribution under the amplitude of 16.5~30.7%, so the theoretical calculated maximum bending moment modification value of 35.65% (slightly higher than the test maximum bending moment modification value of 30.7%) should be credible. Table 5 shows the results of the experimental data and theoretical calculations.

Table 5. Theoretical moment modification values and measured moment modification values of each continuous slab.

Test Piece Number	JLB-1	JLB-2	JLB-3	JLB-4
Test damage load (kN)	24.5	24.65	23.75	23.65
Test amplitude adjustment value	19.3%	25.3%	16.5%	30.7%

The calculation results show that under the loading method studied in this paper, the continuous plate has a bending moment modification limit of 35.65% for a given

load $P_u = 24$ kN, which is credible when combined with the calculation results of the experimental analysis.

4.2. Experimental Phenomena and Analysis of Honeycomb Core Slab and Waffle Slab

(1) Comparative analysis of cracks in honeycomb core slab and waffle slab

Cracks first appear in the middle of both the honeycomb core and waffle slab bottom surfaces, and as the load increases, the cracks develop along the diagonal toward the four corner points. The cracks at the top of the slab are basically parallel to the wall midline except for the cracks near the corner points which are basically perpendicular to the diagonal direction, and this crack pattern is similar to the damage pattern of the four-sided fixed two-way solid slab.

At the same time, these two types of slabs have their own unique characteristics. The first appearance of cracks in the waffle slab is usually in the transverse direction, while for the honeycomb core slab, diagonal cracks are typically observed. This is because the honeycomb core links the ribs in both directions, altering the load transmission mechanism of the slab. In comparison, the T-shaped ribs in a waffle slab are replaced with box-shaped ribs in a honeycomb core slab. This increases the stiffness and reduces deformation, thus delaying the occurrence and progression of cracks. Figures 20 and 21 illustrate the distribution of cracks when the honeycomb core cover and the waffle slab are damaged.



Figure 20. Crack distribution when the honeycomb core slab is damaged.



Figure 21. Distribution of cracks during damage of waffle slab.

For honeycomb core slabs, cracks first appear at the junction of the core mold and ribs under the fifth level of load. Under the sixth level of load, cracks appear along the diagonal direction of the plate at the nodes of the ribs, and the width of these cracks is larger than that at the junction. This indicates that there is relative slip between the honeycomb core mold and the surrounding concrete. However, since the cracking load is relatively large, it suggests that there is good bonding between the honeycomb core and the ribs. After the experimental component is demolished, it is also observed that there is good adhesion between the core mold and the surrounding concrete.

The failure mechanisms of both the four-sided fixed-supported bi-directional waffle slab and the four-sided fixed-supported honeycomb core slab are similar to those of the four-sided fixed-supported bi-directional slabs, i.e., the plastic hinge lines are distributed at 45° along the four corner points. Both the regular service stage and failure stage, as well as the floors, are mainly controlled by the width of cracks.

(2) Comparative analysis of the deformation of honeycomb core slab and waffle slab

The load–deflection curves of the honeycomb core slab and waffle slab are shown in Figure 22. Compared with the waffle slab, the honeycomb core slab has a higher stiffness

and a smaller deflection. In the elastic phase, the mid-span deflection of the honeycomb core slab is only about 35% of that of the waffle slab.

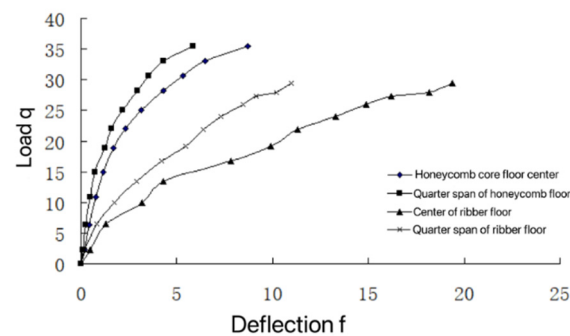


Figure 22. Load–deflection curve of honeycomb core slab and waffle slab.

The mechanical characteristics of honeycomb core slabs are similar to those of bidirectional solid slabs. So the midpoint deflection of the honeycomb core slab is

$$w = \frac{\alpha_f q_k l^4}{D} \quad (47)$$

where α_f is the solid slab elastic parameter of the deflection coefficient, for a uniform load under the action of a four-sided rigid fixed two-way floor, taking the value of the case in Table 6; q_k is the unit area of the plate under constant load and live load with a standard value of the sum; l is the span of the cover, taking the smaller values of l_x and l_y ; and D is the unit width of the cover-equivalent cross-sectional stiffness.

Table 6. Deflection coefficient of four-sided rigid fixed bi-directional floor under uniform load.

l_x/l_y	0.50	0.55	0.60	0.65	0.70	0.75	0.80	0.85	0.90	0.95	1.0
$\alpha_f(10^{-3})$	2.54	2.46	2.37	2.25	2.08	1.96	1.82	1.67	1.52	1.39	1.26

According to Equation (47), the deflection of the slab center can be calculated under various levels of load. The stiffness under the first level of load is considered as reference value 1 to calculate the relative stiffness under different levels of load. From the curve in Figure 23, it can be seen that the stiffness of the honeycomb core slab changes slowly with the load, and the stiffness decreases more uniformly, while the stiffness of the waffle slab decreases faster with the increase in the load, especially in the early loading period when the stiffness of the slab decreases more drastically.

(3) Comparative analysis of bearing capacity of honeycomb core slab and waffle slab

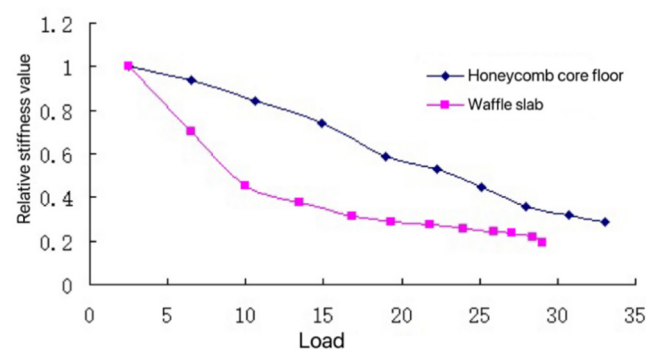


Figure 23. Variation curve of stiffness of honeycomb core slab and waffle slab.

The main factors of the honeycomb core slab where it has a higher bearing capacity than the waffle slab can be briefly summarized as follows:

- (1) Due to the role of the core bottom plate, the width of the pressure zone at the negative bending moment of the slab plate increases (the bottom plate will not crack under pressure in the negative moment zone), the height of the pressure zone decreases, and the effective height of the section increases, thus improving the bearing capacity (about 8%);
- (2) The membrane internal force of the bottom plate assumes part of the load;
- (3) The torsional resistance of the box-shaped section is better than that of the T-shaped section, thus reducing the bending and torsional correlation of the slab;
- (4) The integrity of the honeycomb core slab is better than that of the waffle slab, the internal force is more uniformly distributed, and the material is fully utilized.
- (4) Comparison of internal force and deformation between honeycomb core slab and waffle slab

The equivalent stiffness of the cross-section and the related parameters are substituted into the calculation formula to obtain the internal force of each beam rib and the deflection at the center of the slab under the design load as shown in Table 7 (q is the value of the added uniform load in the table). The numbers of beam ribs in the table are shown in Figure 5. Table 8 shows the measured values and calculated values of deformation in the middle of the span of the honeycomb core slab and waffle slab.

Table 7. Comparison of internal force (kN·m) and deformation (mm) between honeycomb core slab and waffle slab.

	M_{A4}	M_{A3}	M_{A2}	M_{A1}	M'_{A4}	M'_{A3}	M'_{A2}	M'_{A1}	ω_c
Honeycomb core slab	$-0.289q$	$-0.248q$	$-0.189q$	$-0.072q$	$0.146q$	$0.121q$	$0.079q$	$0.009q$	$0.051q$
waffle slab	$-0.301q$	$-0.258q$	$-0.184q$	$-0.083q$	$0.149q$	$0.118q$	$0.078q$	$0.011q$	$0.129q$

Note: M'_{A4} , M'_{A3} , M'_{A2} , and M'_{A1} represent the mid-span bending moment; ω_c represents the deformation in the middle of the span.

Table 8. Measured values and calculated values of deformation (mm) in the middle of the span of both the honeycomb core slab and waffle slab.

	Honeycomb Core Slab				Waffle Slab	
Level	1	2	3	4	1	2
Measured value	0.13	0.39	0.71	1.12	0.34	1.36
Calculate value	0.12	0.33	0.54	0.76	0.31	0.84
Error	7.7%	15.4%	23.9%	32.1%	8.8%	38.2%

From the comparison of the data in the table, it can be seen that the internal force of the honeycomb core slab is slightly smaller than that of the waffle slab in general, and the deflection at the center is reduced substantially (up to 60%), which shows the superiority of the force performance of the honeycomb core cover over the waffle slab.

It should be noted that the method of equivalently converting the honeycomb core floor slabs and densely ribbed floor slabs into orthotropic plates based on the principle of equivalent bending stiffness yields quite ideal results in the elastic stage. However, if the floor slab cracks and enters the plastic stage, the errors in the calculation results will increase, and this method will no longer be applicable.

5. Conclusions

In this paper, the effect of GFRP on the hollow core slab and slab is studied, and a detailed performance comparison and theory are made with the common hollow core slab and slab. The following conclusions are mainly drawn:

- (1) In the load-bearing limit state, when the height of the concrete compression zone meets certain conditions, the GFRP thin-walled tube is able to contribute to the structural strength of the circular tubular hollow slab. This can improve the load-bearing capacity of the section to some extent.
- (2) The energy method is utilized to derive the plastic angle that is required for the GFRP circular tubular hollow continuous slab to satisfy a specific modification. A comparison between the experimental measured values and the theoretical calculated values demonstrates that the theoretical calculation method is both reasonable and feasible. The calculation results reveal that, under the studied loading mode, the continuous slab possesses a credible bending moment modification limit of 35.65% for a given load of 24 kN, as supported by the experimental analysis calculation results.
- (3) The GFRP honeycomb core makes the slab a closed cavity structure and contributes to the stiffness of the slab. In the elastic phase, the deflection at the mid-span of the GFRP honeycomb core slab is significantly lower than that of the waffle slab. Moreover, the presence of the GFRP honeycomb core delays the appearance and development of cracks.

Author Contributions: Conceptualization, W.Y.; methodology, Z.Z.; formal analysis, Z.Y. and Z.Z.; writing—original draft preparation, H.L.; writing—review and editing, Z.Z.; supervision, W.Y.; funding acquisition, W.Y. All authors have read and agreed to the published version of the manuscript.

Funding: This research was funded by the Research Project of Educational Commission of Hunan Province, China grant number [22A0239] and the Talent Recruitment Project of Hunan Province, China grant number [2023TJ-Z17]. And The APC was funded by the Talent Recruitment Project of Hunan Province, China grant number [2023TJ-Z17].

Institutional Review Board Statement: Not applicable.

Informed Consent Statement: Not applicable.

Data Availability Statement: The data are available from the corresponding author on reasonable request.

Acknowledgments: This work was jointly supported by the Research Project of the Educational Commission of Hunan Province, China (grant no. 22A0239), and the Talent Recruitment Project of Hunan Province, China (grant no. 2023TJ-Z17).

Conflicts of Interest: The authors declare no conflict of interest.

References

1. Al-Gasham, T.S.; Hilo, A.N.; Alawsi, M.A. Structural behavior of reinforced concrete one-way slabs voided by polystyrene balls. *Case Stud. Constr. Mater.* **2019**, *11*, e00292. [[CrossRef](#)]
2. Sagadevan, R.; Rao, B.N. Experimental and analytical investigations on two-way flexural capacity of biaxial voided slab. In *Advances in Structural Technologies: Select Proceedings of CoAST 201*; Springer: Singapore, 2021; pp. 233–247.
3. Varshney, H.; Jauhari, N.; Bhatt, H. A Review Study on Bubble Deck Slab. *Int. J. Res. Appl. Sci. Eng. Technol.* **2017**, *5*, 2136–2139. [[CrossRef](#)]
4. Wheeler, H. Flat Plate Voids Slabs: A Lightweight Concrete Floor System Alternative. Master's Thesis, Kansas State University, Manhattan, KS, USA, 2018.
5. Li, H.; Deng, Q.; Zhang, J.; Xia, B.; Skitmore, M. Assessing the life cycle CO₂ emissions of reinforced concrete structures: Four cases from China. *J. Clean. Prod.* **2019**, *210*, 1496–1506. [[CrossRef](#)]
6. Zhang, H.; Huang, W.; Liu, B.; Han, C.; Li, Q.; Chen, C. Flexural behavior of precast concrete hollow-core slabs with high-strength tendons. *J. Build. Eng.* **2022**, *59*, 105050. [[CrossRef](#)]
7. Kankeri, P.; Prakash, S.S. Experimental evaluation of bonded overlay and NSM GFRP bar strengthening on flexural behavior of precast prestressed hollow core slabs. *Eng. Struct.* **2016**, *120*, 49–57. [[CrossRef](#)]

8. Elhashimy, A.M.; Tawhed, W.F.; Agamy, M.H. Behavior of Hollow Core Slabs Reinforced with GFRP Prestressing Bars. *Int. J. Eng. Adv. Technol.* **2020**, *9*, 1796–1803. [\[CrossRef\]](#)
9. Lee, Y.J.; Kim, H.G.; Kim, M.J.; Kim, D.H.; Kim, K.H. Shear performance for prestressed concrete hollow core slabs. *Appl. Sci.* **2020**, *10*, 1636. [\[CrossRef\]](#)
10. Zhang, X.; Zhang, Y.; Shan, R.; Bai, Y.; Zhang, Z. Application on bending performance of annular concrete-filled steel tube stent. *J. Constr. Steel Res.* **2020**, *168*, 105984. [\[CrossRef\]](#)
11. Ferdous, W.; Bai, Y.; Almutairi, A.D.; Satasivam, S.; Jeske, J. Modular assembly of waterretaining walls using GFRP hollow profiles: Components and connection performance. *Compos. Struct.* **2018**, *194*, 1–11. [\[CrossRef\]](#)
12. Lai, M.; Binhowimal, S.; Hanzic, L.; Wang, Q.; Ho, J. Dilatancy mitigation of cement powder paste by pozzolanic and inert fillers. *Struct. Concr.* **2020**, *21*, 1164–1180. [\[CrossRef\]](#)
13. Lai, M.; Hanzic, L.; Ho, J.C. Fillers to improve passing ability of concrete. *Struct. Concr.* **2018**, *20*, 185–197. [\[CrossRef\]](#)
14. Cho, S.; Na, S. Evaluation of the Flexural Performance and CO₂ Emissions of the Voided Slab. *Adv. Mater. Sci. Eng.* **2018**, *2018*, 3817580. [\[CrossRef\]](#)
15. Kang, S.M.; Kim, J.W.; Choi, K.K.; Park, H.G. Shear behavior investigation of biaxial hollow slabs through non-linear FE analysis. *J. Archit. Inst. Korea Struct. Constr.* **2016**, *32*, 3–13. [\[CrossRef\]](#)
16. Amoushahi Khouzani, M.; Zeynalian, M.; Hashemi, M.; Mostofinejad, D.; Farahbod, F. Study on shear behavior and capacity of biaxial ellipsoidal voided slabs. *Structures* **2020**, *27*, 1075–1085. [\[CrossRef\]](#)
17. Nguyen, T.H.; Tan, K.H.; Kanda, T. Investigations on web-shear behavior of deep precast, prestressed concrete hollow core slabs. *Eng. Struct.* **2019**, *183*, 579–593. [\[CrossRef\]](#)
18. Sagadevan, R.; Rao, B.N. Effect of void former shapes on one-way flexural behaviour of biaxial hollow slabs. *Int. J. Adv. Struct. Eng.* **2019**, *11*, 297–307. [\[CrossRef\]](#)
19. Chung, J.H.; Jung, H.S.; Bae, B.I.; Choi, C.S.; Choi, H.K. Two-way flexural behavior of donut-type voided slabs. *Int. J. Concr. Struct. Mater.* **2018**, *12*, 3817580. [\[CrossRef\]](#)
20. Gong, C.; Hou, Z.X.; Cheng, G.Z.; Wang, G.; Chen, Y.F. Bending Capacity of Biaxial-Hollow RC Slab with Asymmetric Steel Beams. *Adv. Steel Constr.* **2020**, *16*, 321.
21. Ferdous, W.; Almutairi, A.D.; Huang, Y.; Bai, Y. Short-term flexural behaviour of concrete filled pultruded GFRP cellular and tubular sections with pin-eye connections for modular retaining wall construction. *Compos. Struct.* **2018**, *206*, 1–10. [\[CrossRef\]](#)
22. Azad, A.K.; Hakeem, I.Y. Flexural behavior of hybrid hollow-core slab built with ultra high performance concrete faces. *Mater. Struct.* **2016**, *49*, 3801–3813. [\[CrossRef\]](#)
23. Khouzani, M.A.; Zeynalian, M.; Hashemi, M.; Mostofinejad, D.; Farahbod, F. Investigation of flexural and shear behaviors of biaxial voided slabs containing steel cages. *Struct. Concr.* **2020**, *21*, 291–302. [\[CrossRef\]](#)
24. Valivonis, J.; Skuturna, T.; Daugevic, M.; Sneideris, A. Punching shear strength of reinforced concrete slabs with plastic void formers. *Constr. Build. Mater.* **2017**, *145*, 518–527. [\[CrossRef\]](#)
25. Chung, L.; Lee, S.H.; Cho, S.H.; Woo, S.S.; Choi, K.K. Investigations on Flexural Strength and Stiffness of Hollow Slabs. *Adv. Struct. Eng.* **2016**, *13*, 591–602. [\[CrossRef\]](#)
26. Li, C.; Xian, G.; Li, H. Effect of postcuring immersed in water under hydraulic pressure on fatigue performance of large-diameter pultruded carbon/glass hybrid rod. *Fatigue Fract. Eng. Mater. Struct.* **2019**, *42*, 1148–1160. [\[CrossRef\]](#)
27. Yang, Y.; Xian, G.; Li, H.; Sui, L. Thermal aging of an anhydride-cured epoxy resin. *Polym. Degrad. Stab.* **2015**, *118*, 111–119. [\[CrossRef\]](#)
28. Zhang, Z.; Paul, C.P.; Panda, B.; Huang, Y.; Garg, A.; Zhang, Y.; Zhang, W. Assessment of flexural and splitting strength of steel fiber reinforced concrete using automated neural network search. *Adv. Concr. Constr.* **2020**, *10*, 81–92.
29. Guo, R.; Xian, G.; Li, C.; Hong, B. Effect of fiber hybrid mode on the tension–tension fatigue performance for the pultruded carbon/glass fiber reinforced polymer composite rod. *Eng. Fract. Mech.* **2022**, *260*, 108208. [\[CrossRef\]](#)
30. Nguyen, H.T.; Li, Y.; Tan, K.H. Shear behavior of fiber-reinforced concrete hollow-core slabs under elevated temperatures. *Constr. Build. Mater.* **2021**, *275*, 121362. [\[CrossRef\]](#)
31. Chung, J.H.; Jung, H.S.; Choi, H.K. Flexural Strength and Stiffness of Donut-Type Voided Slab. *Appl. Sci.* **2022**, *12*, 5782. [\[CrossRef\]](#)
32. Tynski, E. Experimental Study of Hollow FRP Sections under Bending for Use as Bridge Decking. Master’s Thesis, Dalhousie University, Halifax, NS, Canada, 2020.
33. Al-Fakher, U.; Manalo, A.; Ferdous, W.; Aravinthan, T.; Zhuge, Y.; Bai, Y.; Edoo, A. Bending behaviour of precast concrete slab with externally flanged hollow FRP tubes. *Eng. Struct.* **2021**, *241*, 112433. [\[CrossRef\]](#)
34. Wu, Y.; Cheng, S.; Ragaby, E. Effectiveness of a Novel Technique in Strengthening Web-Shear Capacity of Prestressed Hollow Core Slabs Using Externally Bonded FRP Sheets. *J. Compos. Constr.* **2017**, *21*, 04016060. [\[CrossRef\]](#)
35. Yang, W.J.; Zhang, Z.H.; Liu, C.W. Experimental Study on Mechanical Property of Stiffening-ribbed-hollow-pipe Cast-in place Reinforced Concrete Girderless Slab. *J. Civ. Eng. Archit.* **2009**, *3*, 59–69.
36. Li, F. Study of Function of Pipe under Static Loading on Cast-in-Place Hollow Concrete Slab. Master’s Thesis, Tianjin University, Tianjin, China, 2004. (In Chinese).
37. Zhao, S.B.; Sun, X.Y.; Li, C.Y. Flexural Toughness of Steel Fiber Reinforced High-strength Concrete. *J. Build. Mater.* **2003**, *6*, 95–99.
38. Zhu, B.L.; Dong, Z.X. *Nonlinear Analysis of Reinforced Concrete*, 1st ed.; Tongji University Press: Shang Hai, China, 1985; pp. 42–45. (In Chinese)

39. *JTG D62-2004*; Standard of Communication Department of P.R.C. The People's Communications Press: Beijing, China, 2004. (In Chinese)
40. Wang, C.Z.; Teng, Z.M. *Reinforced Concrete Structure Theory*, 1st ed.; Chinese Architecture Industry Press: Beijing, China, 1985; pp. 369–372. (In Chinese)
41. Zhang, Z.H. The Research on the GBF Reinforced Concrete Slabs and Its Application to the Bridge Engineering. Master's Thesis, Changsha University of Science and Technology, Changsha, China, 2006. (In Chinese)

Disclaimer/Publisher's Note: The statements, opinions and data contained in all publications are solely those of the individual author(s) and contributor(s) and not of MDPI and/or the editor(s). MDPI and/or the editor(s) disclaim responsibility for any injury to people or property resulting from any ideas, methods, instructions or products referred to in the content.